ADVANCED OPTICAL MATERIALS
www.advopticalmat.de

High-Efficiency Broadband Mid-Infrared Flat Lens

*Alireza Safaei, Abraham Vázquez-Guardado, Daniel Franklin, Michael N. Leuenberger, and Debashis Chanda**

Integrated photonic circuits and infrared imaging systems demand compact optical components. Dielectric diffractive optics enables miniaturization of the curved refractive optics into planar structure by encoding phase over a 2D plane. However, in the mid-infrared wavelength range, such engineered dielectric surfaces are not efficient, because optically transparent dielectric scatterers with high index contrast in the mid-infrared spectral range suffer from low bandwidth and high thermal noise in long wavelengths. Here, a planar optical lens based on ultrathin gold plasmonic nanostructure operating in the mid-infrared spectral range is demonstrated. The design enables subwavelength focusing beyond the Abbe-Rayleigh diffraction limit while maintaining high transmission efficiency (≈60%) with excellent agreement between electromagnetic simulations and confocal measurements. Single and bilayer flat lenses designed for subwavelength polarization-dependent line and polarization-independent point focusing, respectively, are demonstrated. Such geometry-defined tunable optical response overcomes the challenges associated with the unavailability of mid-infrared transparent materials for low footprint planar integration with thermal imaging systems.

1. Introduction

Conventional optical elements such as lenses, waveplates, and polarizers function by adding gradual phase delays to the propagating light. The accumulated phase by propagating light through a lens is defined as $\Delta\varphi = \Delta n\,|\mathbf{k}|\,\Delta l$, where Δn is the refractive index difference between the surrounding medium and the lens, $|\mathbf{k}|$ is the magnitude of the wavenumber, and Δl is the propagation distance. For conventional refractive lenses, Δn is small, which means that the thicknesses of these dielectric optical components need to be much larger than the wavelength of incoming light to accumulate 0 to π phase shifts. That means subwavelength compact planar geometry is not possible in conventional lenses making optical systems bulky. Furthermore, conventional lenses are limited by optical aberrations (e.g., spherical and chromatic) and diffraction limit.[1] The Abbe-Rayleigh diffraction limit is a natural obstacle in conventional optical lenses due to the far-field interference and absence of near-field.[2] Various planar lenses have been demonstrated following the diffractive optics concept of phase control based on dielectric scatterers on a 2D plane.[3–9] However, in the mid-infrared wavelength range (3–16 μm), such engineered dielectric surfaces are elusive due to the low spectral bandwidth[8,9] and high thermal noise in long wavelengths.[10,11]

In contrast, plasmonic nanoantennas[12–17] enable abrupt change in phase, amplitude, and polarization of the incident light using subwavelength optical scatterers on a planar surface. Such control of phase according to the Huygens principle[18] allows the formation of arbitrary wavefront shapes enabling subwavelength focusing.[3–5] Spatially distributed plasmonic nanoantennas suppress higher diffraction orders and concentrate the incident light beam beyond the Abbe-Rayleigh diffraction limited focal point.[19–22] In addition, possibility of the optical impedance matching with the free space by the patterned plasmonic interface reduces back scattering, leading to higher transmission efficiency.[5,23] Going beyond the Abbe-Rayleigh diffraction limit requires the involvement of evanescent fields with large spatial frequency components which is possible by plasmonic nanoantennas, enabling subwavelength resolution capability going beyond the current imaging technologies.[2,14,22,24,25]

Here, we propose and experimentally demonstrate an ultrathin flat lens working in the mid-IR spectral range with geometrically tunable focal length and subwavelength focusing ability. The transmission efficiency of this flat lens is substantially higher compared with other reported plasmonic lenses due to the low metallic fill-fraction and the geometry.[14–16,26,27] The biggest limitation of dielectric as well as metallic flat lenses is the bandwidth of operation due to the inherent narrowband resonance.[8,9] Previously, reported plasmonic flat lenses were limited to $\lambda \approx 1.0$–1.9 μm,[15] ≈5.2–9.9 μm,[16] and $\lambda \approx 5$–10 μm,[14] operation bandwidths in the infrared spectral range. None of these works reported the most critical lens

A. Safaei, D. Franklin, Prof. M. N. Leuenberger, Prof. D. Chanda
Department of Physics
University of Central Florida
Orlando, FL 32816, USA
E-mail: debashis.chanda@ucf.edu
A. Safaei, A. Vázquez-Guardado, D. Franklin, Prof. M. N. Leuenberger, Prof. D. Chanda
NanoScience Technology Center
University of Central Florida
Orlando, FL 32816, USA
A. Vázquez-Guardado, Prof. D. Chanda
CREOL
The College of Optics and Photonics
University of Central Florida
Orlando, FL 32816, USA

DOI: 10.1002/adom.201800216

parameter transmission efficiency. In contrast, our proposed lens offers a wide operation bandwidth due to its gradient design. For the optimum design, the experimentally measured transmission remained >70% over the entire 4–10 µm mid-IR spectral range, which promises further improvement in broadband transmission efficiency with improved fabrication procedures. Single (polarization dependent) and bilayer (polarization independent) designs enable the polarization degree of freedom as well as tunable line and point focusing, respectively. Furthermore, such geometry-defined tunable optical response overcomes the challenges associated with the unavailability of mid-infrared transparent materials for low footprint planar integration with thermal imaging systems.

Controlling phase response on a 2D plane based on polar dielectric scatterers is well known in the literature as diffractive optics.[3–6,21,28] However, as pointed out earlier, in the mid-IR spectral range, most dielectrics are nontransparent. We demonstrate coupled gradient gold disk arrays as low loss broadband focusing element with a plasmon resonance in the mid-infrared spectral range, far away from the natural plasmon resonance of gold. Our proposed gold arrays work as follows. The incident light beam excites surface plasmons on the metallic nanostructure with a specified diameter (L_{res}), leading to coupling of the incident light beam to the array like an optical antenna. Strong interaction between the incident light beam and surface plasmon leads to an abrupt phase change of the scattered electric field.[5,13,15,16,19,29–38] Excitation of surface plasmons is due to the charge oscillation on the metallic elements driven by the incident electric field, and at the plasmon resonance frequency, the driving optical field is in phase with the induced current. The change in the length of the nanostructure gives rise to the change in the resonance frequency, and consequently, the excited current leads or lags the incident field. A 2D pattern comprised of gradient gold disks with optimum diameter ratio creates a spatially varying phase response, which enables the modulation of the optical wavefront such that the energy is focused in forward direction.[5,14]

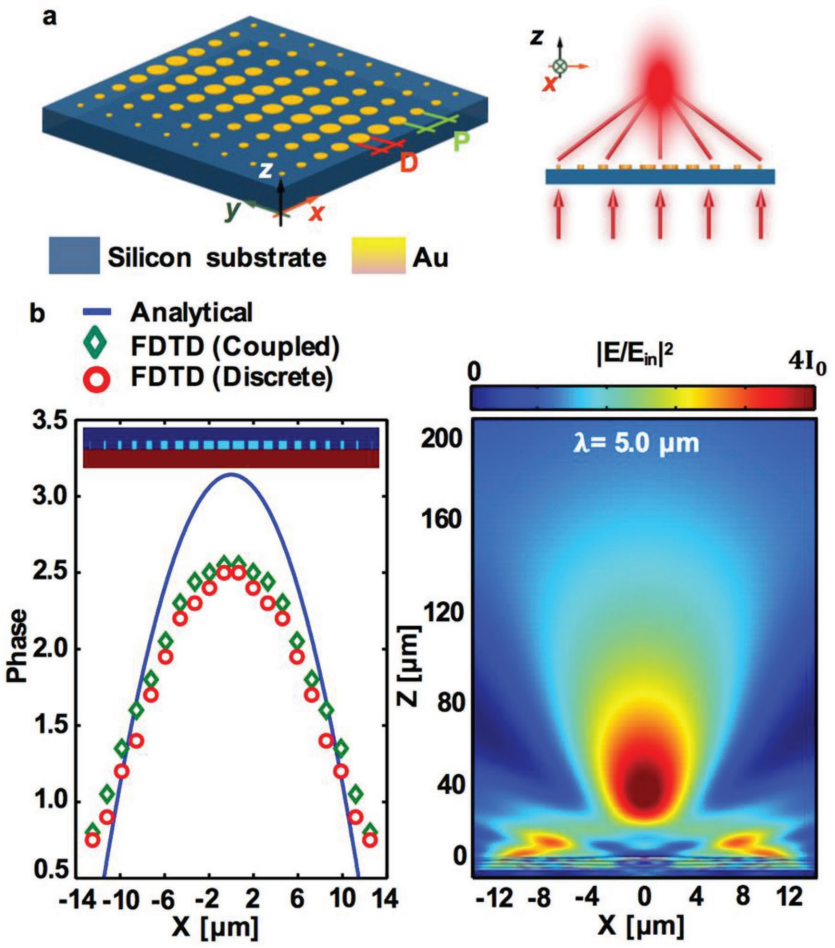

Figure 1. Gradient phase shift and focusing. a) (left) Schematic of the polarization-dependent plasmonic lens. The period (P) is constant and disk diameters (D) are variable. (right) Schematic of position-dependent phase shifts by different disk arrays which lead to curved phase front. b) (left) Phase shift of the incident light by coupled and detached disk arrays. The solid blue line shows the analytical phase shift for $F = 40$ µm and $\lambda = 5.0$ µm derived from Equation (1). Top inset is the side view of the simulated nanostructure. (right) FDTD result of the focusing effect for Y-polarized light incident from bottom side of plasmonic lens with $P = 1.3$ µm, $D_0 = 1.0$ µm, and $\Delta D = 0.1$ µm at $\lambda = 5.0$ µm.

2. Results and Discussion

2.1. Spatially Varying Gradient Phase Response

Figure 1a shows the proposed plasmonic lens, which is composed of an adiabatically tapered ultrathin (45 nm) gold nanodisk array along one direction. Such a discrete gradient subwavelength gold disk array functions like an optical antenna array by concentrating the electromagnetic energy to a given direction based on the excitation of surface plasmons. The abrupt phase shift originates from the excitation of two nondegenerate eigenmodes on the asymmetric pattern. The change in the in-plane size of the nanodisk elements for a constant period P changes the phase of the scattered optical field, thus enabling the creation of a curved phase front. For the line focus, the disk is arranged in a 2D array with a gradual change in diameter only in one direction, as shown in Figure 1a (left). The central 1D disk array adds the maximum phase shift to the scattered electromagnetic wave due to the excitation of the surface plasmon at the resonance wavelength (λ_{res}). The gradual decrease in the size of elements along the orthogonal direction gives rise to a weaker driving current and a lower phase delay, leading to the creation of a cylindrical wavefront. It means that in order to have a perfect optical flat lens operating at a specified wavelength (λ_m), the central arrays should be designed

such that $\lambda_{res} = \lambda_m$. Such a gradient pattern creates a spatially varying phase response, giving rise to the focusing effect, as shown schematically in Figure 1a (right).

This single layer design acts as a far-field cylindrical optical flat lens at mid-IR frequencies for the polarization perpendicular to the direction of the diameter variation if the spatial distribution of the optical phase response (φ) follows[5,21,39]

$$\varphi(x) = 2n\pi + \frac{2\pi f}{\lambda} - \frac{2\pi\sqrt{f^2 + x^2}}{\lambda} \quad (1)$$

where x is position, n is an integer, f denotes the focal length, and λ stands for the wavelength of the incident light. To study the behavior of such a lens on-resonance and off-resonance, two flat lenses with different periods ($P = 1.3$ μm and $P = 2$ μm) for a constant diameter difference of $\Delta D = (D_2 - D_1) = 100$ nm and constant central disk diameter of $D_0 = 1$ μm are designed. The flat lens with period $P = 1.3$ μm has a resonance wavelength at $\lambda = 4.56$ μm, and the one with period $P = 2.0$ μm at $\lambda = 6.5$ μm. The resonance wavelength of a lens pattern corresponds to the dip in the far-field transmission spectra which is same as the dip in the transmission efficiency at the focal point ($\lambda_{res} = 4.56$ μm for $P = 1.3$ μm and $\lambda_{res} = 6.5$ μm for $P = 2.0$ μm), as shown with a dashed line in Figure 6a. Figure 1b (left) compares the required phase defined by Equation (1) with the extracted phase shift of the flat lens with period $P = 1.3$ μm. Finite-difference time-domain (FDTD) simulation is used to estimate the phase from the z-component of the electric field for both the 1D coupled array (in the direction of diameter variation) and the 2D coupled array. From this FDTD phase prediction, it can be concluded that the coupling is negligible along the direction perpendicular to the diameter variation. The focal length f used in Equation (1) for this design is derived from the FDTD simulation. To calculate the phase response corresponding to each array element analytically, the Lippmann–Schwinger equation[40–44] along with the geometry-dependent polarizability of each element (α)[45] can be used to derive the radiated electric field and consequently the phase shift. The FDTD-predicted field intensity distribution demonstrating focusing as predicted is shown in Figure 1b (right). The slight mismatch between the ideal phase distribution and the numerically simulated phase due to the nanostructure diameter and the location variation, which do not exactly follow Equation (1), result in smaller side lobes in the focal volume, as can be seen in Figure 1b (right).

2.2. Lens Design Parameters

The figure of merit of any lens is defined by bandwidth, efficiency, focal length, and depth of focus. The resistive plasma loss and adiabatic shape variation of this low-Q system makes the proposed design broadband in nature, which enables the lens to operate across a wide wavelength range as predicted by the FDTD simulation in **Figure 2**a. The plasmonic surface possesses the unique ability to impedance match with the free-space which reduces back reflection and consequently increases the transmission efficiency. In addition, the efficiency of the designed lens depends on the metallic plasma loss, the period, the diameter, and the thickness of metallic elements of the 2D pattern.

The size of the focal point is characterized by the full width half maximum with respect to the wavelength (FWHM/wavelength), which plays the crucial role in energy concentration

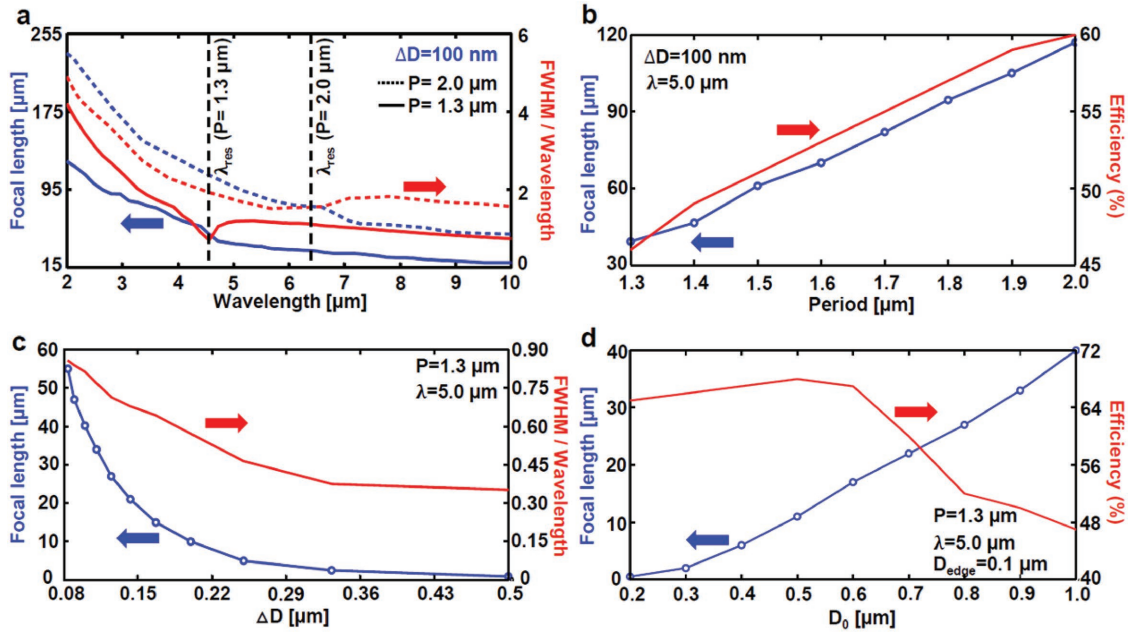

Figure 2. Focal length and efficiency variation. a) Focal length (blue line-circle) and FWHM/wavelength (red line) as functions of the wavelength of the incident light for $P = 1.3$ μm, $\Delta D = 0.1$ μm, and $D_0 = 1$ μm. b) Focal length (blue line-circle) and efficiency (red line) as functions of the pattern period for $\Delta D = 0.1$ μm, $D_0 = 1$ μm, and $\lambda = 5.0$ μm. c) Focal length (blue line-circle) and FWHM/wavelength (red line) as functions of the diameter difference for $P = 1.3$ μm, $D_0 = 1$ μm, and $\lambda = 5.0$ μm. d) Focal length (blue line-circle) and efficiency (red line) as functions of the central diameter (D_0) for $P = 1.3$ μm, $D_{edge} = 0.1$ μm, and $\lambda = 5.0$ μm.

at that point and consequently the resolving power of our proposed plasmonic lens. For the present design, the FWHM/wavelength is a decaying function of wavelength, reaching the minimum value at the resonance wavelength (λ_{res} = 4.56 μm) of the nanostructure and becomes less than 1, subwavelength concentration, for higher wavelengths, as shown in Figure 2a. Figure 2a further shows that our proposed flat lens has chromatic aberration for lower wavelengths (<λ_{res}), but has almost constant focal length at higher wavelengths (>λ_{res}), thereby minimizing the chromatic aberration. These aberrations are much smaller compared with other reported flat lenses.[46,47]

Figure 2b shows the predicted efficiency of the flat lens as a function of period P for a fixed differential diameter ΔD = 100 nm. The increase in period P of this 2D array not only enhances the efficiency but also increases the focal length linearly. The larger the period P, the lower is the metallic fill-fraction for a constant ΔD, which reduces loss and hence leads to a higher transmission efficiency. On the other hand, an increase in ΔD at fixed period P and wavelength (λ = 5.0 μm) leads to a sharper change in the diameter and the phase, giving rise to subwavelength concentration FWHM/wavelength (<1) due to involvement of near-field interference and shorter focal length, as can be seen from Figure 2c. The increase in the central diameter (D_0) at fixed period (P = 1.3 μm), wavelength (λ = 5.0 μm), and the edge diameter (diameter of the last disk, D_{edge} = 100 nm) gives rise to larger focal length and lower transmission efficiency, as can be seen from Figure 2d. To evaluate the chromatic aberration in Figure 2a, a fixed image plane position at the focal point of the resonance wavelength λ_{res} is used as the reference, and the FWHMs corresponding to the different wavelengths are calculated at this plane. But in Figure 2c, the FWHM/wavelength are calculated at the focal point correspond to each ΔD at λ_m = 5 μm.

From Figure 2, it can be concluded that the focal length is a linear function of the period P (Figure 2b), a power function of ΔD (Figure 2c) and a power function of D_0 (Figure 2d), which can be combined into: $F = 113\ (P) - 109.6$, $F = 0.9071(\Delta D)^{-1.676} - 3.032$, and $F = 44.13(D_o)^{-1.522} - 4.193$. This set of equations can be easily used to design flat lenses with variable focal length. Based on limitations of the lithography, if we assume ΔD_{min} = 10 nm and D_{edge} = 100 nm, the largest flat lens size for P = 1.3 μm is ≈300 μm and for P = 2.0 μm is ≈800 μm. Increasing the period P and D_0 gives larger lens sizes, and the corresponding focal length can be calculated using the abovementioned set of equations.

According to Equation (1), the focal length depends on the phase shift profile, means $\varphi(x)$ versus x. The phase shift of a nanoantenna element is a linear function of period P and nonlinear function of diameter D, as seen from Figure 4 which is extracted from FDTD simulation. Varying the period while keeping other parameters constant means only the positions of the nanoantenna elements are varying linearly ($x \propto P$), but the number and size of elements are constant. It means according to Equation (1) and Figure S6a in the Supporting Information, for the zeroth-order (n = 0), the focal length should be a linear function of period P, too ($f \propto P$). Unlike the period, as shown in Figure S6b in the Supporting Information, the phase change is a nonlinear function of diameter D. Changing D_0 and ΔD for constant period P means the number and the size of nanoantenna elements are being changed, while x profile is constant. So, according to Equation (1), the focal length f is a nonlinear function of D_0 and ΔD.

2.3. Polarization-Dependent Flat Lens

To study experimentally the effect of the period P, transmission efficiency and field intensity profile, two flat lenses with different periods (P = 1.3 μm and P = 2.0 μm) are fabricated and measured. To increase the overall size of the lens, there can be more than one nanoantenna element with the same diameter instead of gradual decrease in the diameters while maintaining small periods (P < 2 μm) for sufficient near-field interactions. The scanning electron microscope (SEM) images of these two lenses with D_0 = 1 μm, D_{edge} = 100 nm, ΔD = 100 nm, and gold thickness of 45 nm are shown in **Figure 3**a-left (P = 1.3 μm) and 3a-right (P = 2 μm). The diffraction-limited confocal measurement technique is used to scan the spatial field intensity. A plane wave light beam with large spot size and uniform power after passing through a linear polarizer, band pass filter (λ_c = 5.0 μm with bandwidth of 70.0 nm) and a pinhole impinges on the sample and a high numerical aperture objective lens (NA ≈ 0.9) is coupled to a Fourier transform infrared (FTIR) spectrometer to collect photons. A 3D automatic stage is used to change the position of the flat lens sample to scan the focal point, and the light is collected using an objective lens and a mercury cadmium telluride (MCT) photodetector, as schematically shown in Figure S1 in the Supporting Information.

The applied mesh in FDTD simulation is 10 nm in x–y direction and 5 nm in z direction. The intensity accuracy is 0.01 (1/100 I_0). In the measurement, the focal spot of the objective lens is ≈6 μm and the step size of the 3D stage is 100 nm. A high-sensitive MCT photodetector working at 77 °C is used for photon collection.

Figure 3b,c compares the FDTD predicted and the measured field intensity in the cross-section of the focal volume at the x–y plane (top view) for the two lenses, respectively. Since the single-layer flat lens can only focus the TE mode light, there is a focal line instead of focal point, and the results show very good agreement between the FDTD prediction and experimental measurement. From these plots, it can also be observed that the larger period P gives rise to larger FWHM. The increase in the period P decreases the metallic fill-fraction and consequently the plasmonic light–matter interactions. This in turn reduces the amount of transmitted light which accumulates phase shift, leading to a larger focal volume or FWHM.

For quantitative comparison, the simulated and measured field intensity in the cross-section of the focal line along the y-axis are overlaid in Figure 3c-left (P = 1.3 μm) and 3d-right (P = 2.0 μm), which show a good match between simulation and measurement for both lenses. In order to reveal the focal volume, the cross-section of the focal line in the y–z plane (side view) is scanned and compared with the FDTD predictions, as shown in **Figure 4**a,b for both patterns (P = 1.3 μm and P = 2.0 μm). The presence of side lopes is due to the mismatch between the ideal phase predicted by Equation (1) and the actual phase response of the designed plasmonic pattern. Similar to the cross-section of the field intensity in y-direction (Figure 3),

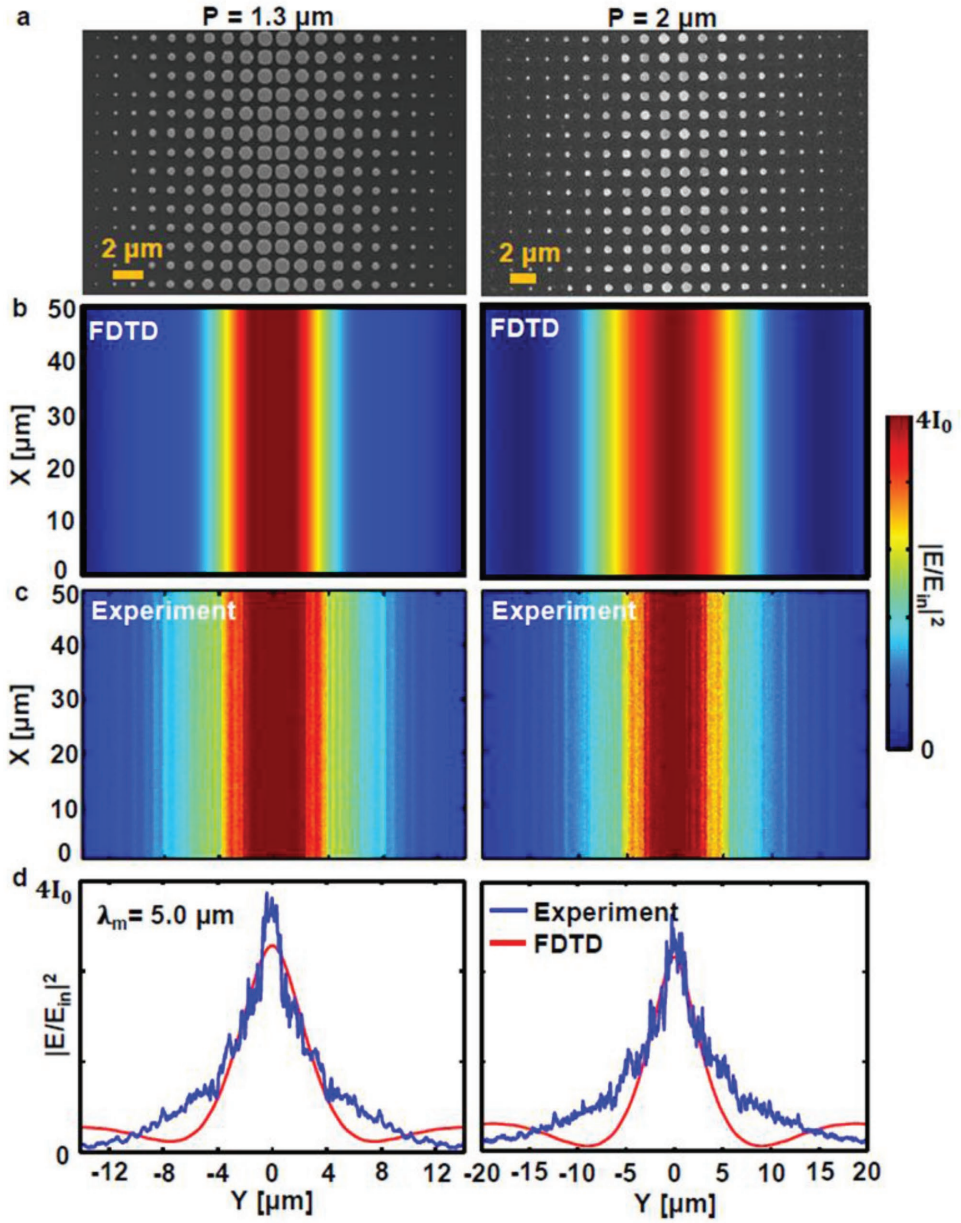

Figure 3. SEM image and top view of electric field intensity at focus of the single-layer flat lens. a) SEM image of the plasmonic lens with the period of $P = 1.3$ μm (left) and $P = 2.0$ μm (right). The simulated (b) and the measured (c) cross-sections of the light field intensities in the *X*–*Y* plane for the plasmonic lenses with $P = 1.3$ μm (left) and $P = 2.0$ μm (right). d) Comparison of the simulated (red) and measured (blue) of the cross-sections of the light intensities along the *Y*-axis for the patterns with $P = 1.3$ μm (left) and $P = 2.0$ μm (right). The operating wavelength is $\lambda_m = 5.0$ μm.

the simulated and measured field intensity along the *z*-axis is overlaid in Figure 4c-left ($P = 1.3$ μm) and 4c-right ($P = 2.0$ μm) with good agreement for both periods. Minor discrepancies are mainly due to the fabrication tolerances, finite diffraction-limited confocal measurement, and the IR detector shot noise.

2.4. Polarization-Independent Flat Lens

The unique feature of the proposed design is that when two such lenses are stacked together with an optimum spacing between them, as schematically shown in **Figure 5**a (top), the resulting bilayer flat lens with 90° rotated layers functions as a polarization-independent point focusing lens with the ability of funneling both TE and TM modes of the incident light. The double-layer lens has two main advantages compared with concentric design. The first one is that it makes it possible to control the focal length for each polarization, independently, which gives a great degree of freedom to design novel polarization-dependent flat lens. Possibility of removing oblique and coma aberrations is another advantage of this design. The second layer can be designed such that

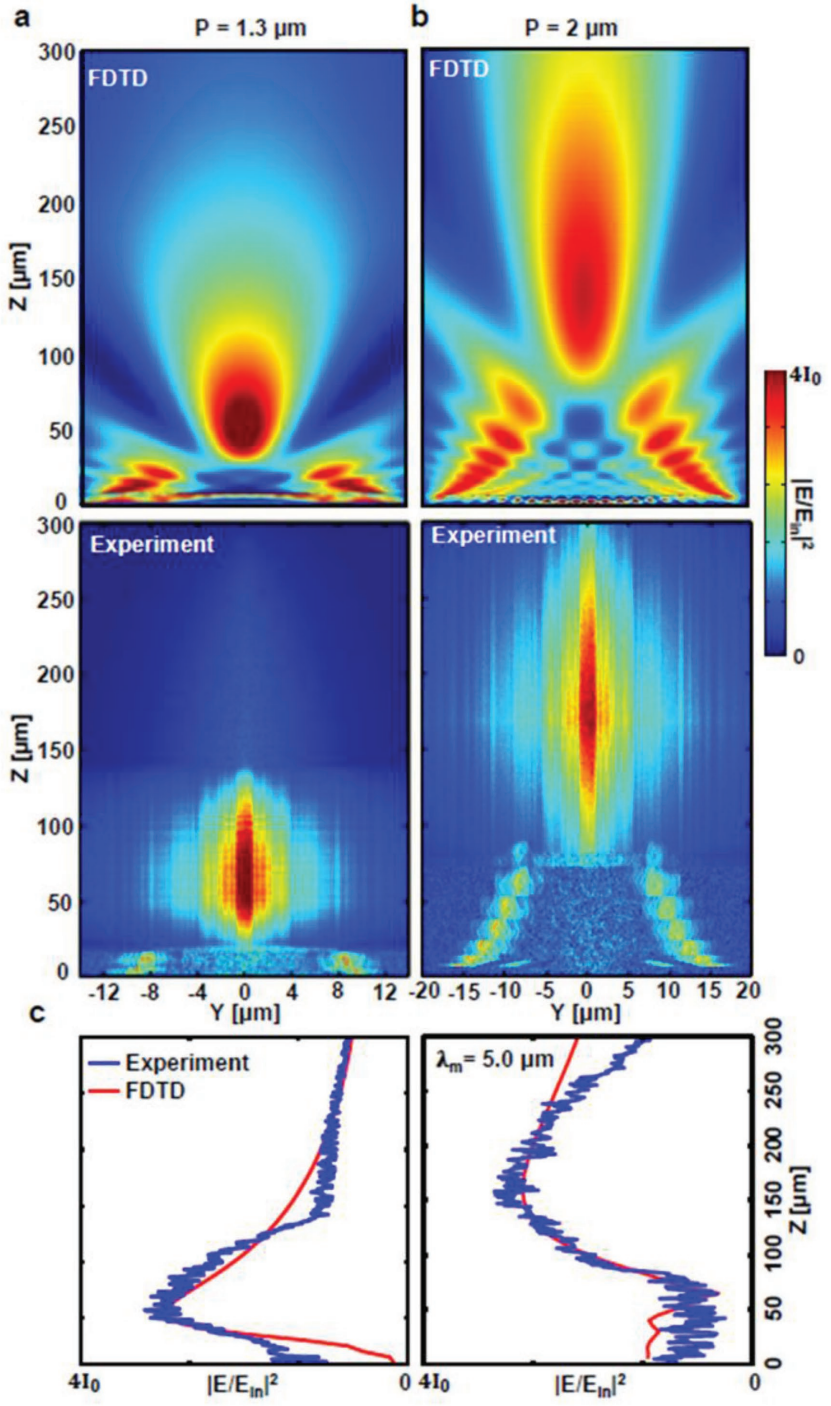

Figure 4. Focal point measurement of the single-layer flat lens. The simulated (a) and the measured (b) cross-section of the light field intensity in the *Y*–*Z* plane for the plasmonic lens with $P = 1.3$ μm (left) and $P = 2.0$ μm (right). c) Comparison of the simulated (red) and measured (blue) cross-section of the light intensity along the *Z*-axis for the patterns with $P = 1.3$ μm (left) and $P = 2.0$ μm (right). The operating wavelength is $\lambda_m = 5.0$ μm.

the rays coming from off-axis light source do not direct away from the optical axis.

The optical image of the fabricated bilayer lens is shown in Figure 5a (middle). Since the separation distance between these two layers is 200 nm, their focal lengths are almost the same, which leads to the creation of a single focal point for an arbitrary linearly polarized light. Furthermore, the decrease in the separation distance does not have a prominent effect on the focal length, which means that the far-field coupling between these layers does not change their focal lengths substantially, but enhances the transmission efficiency a bit, as can be seen from Figure 5a (bottom) and figure S5 in the Supporting Information.

Figure 5b,c compares the cross-section of the simulated and measured field intensity in the *x*–*y* plane (top view) for 45° linear polarized normal incident light. Comparison of Figure 5b,c not only proves the polarization independency of the bilayer flat lens but also shows that the increase in the period *P* gives rise to larger focal volume, similar to the single-layer lens. In Figure 5, the simulated focal points are close to circle, while the measured ones look like a cross-like. There are two reasons for this effect which are related to the fabrication. The first one is the misalignment between the first and second layers which creates discrepancy between simulation and the fabrication. Another reason is that the electron beam lithography system for writing any pattern needs to find the interface by using a laser beam. But due to the nonreflective dielectric spacer on top of the first layer, it finds the interface improperly. It means the second layer is a little bit different from the perfect pattern leading to the discrepancy between the simulation (ideal circle) and measurement (cross-like).

Figures S3 and S4 in the Supporting Information show the simulated and measured cross-sectional field intensity in the *y*–*z* and *x*–*z* planes (side view), which clearly show the same focal length and focus pattern for the perpendicular planes, thereby proving the polarization independency of such a bilayer flat lens. Comparing Figures 3–5 and Figures S3–S4 in the Supporting Information, it is evident that the bilayer lens further reduces the FWHM due to the double excitation of plasmon resonances passing through two layers (FWHM/wavelength = 1.03/0.87 [single layer/bilayer] for $P = 1.3$ μm and = 1.20/1.05 [single layer/bilayer] for $P = 2.0$ μm at $\lambda = 5.0$ μm).

Any type of flat lens with continuous or discrete phase distribution has the monochromatic aberration like coma for the oblique or nonnormal illumination. It means for an ideal Airy disc object, the resultant image would be a comet-like spot similar to other singlet lens. For having

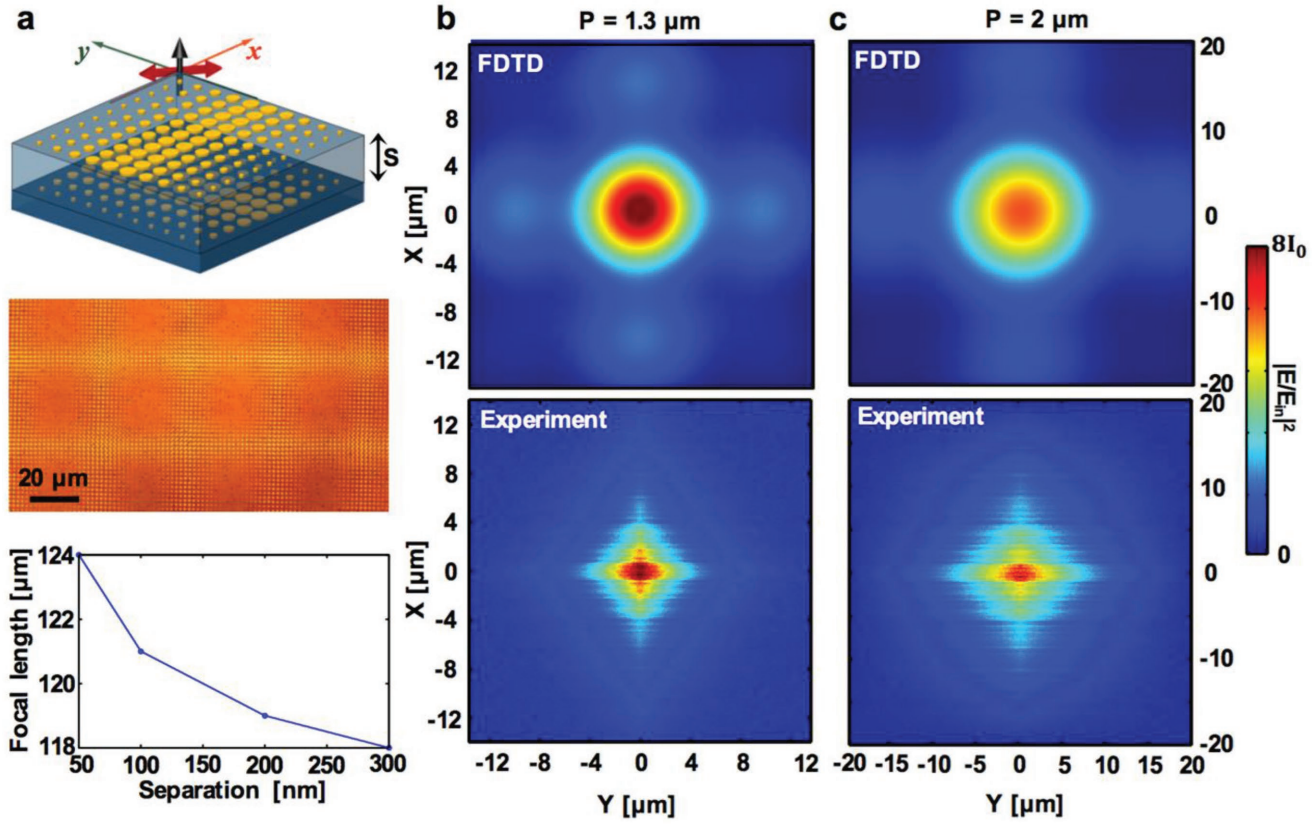

Figure 5. Focal point measurement of the polarization-independent bilayer flat lens. a) (top) The schematic of the bilayer plasmonic lens in presence of incident linear 45°-polarized light. (middle) The optical image of the fabricated bilayer plasmonic lens. (bottom) Focal length as function of the separation distance of bilayer plasmonic lens for $P = 2.0$ μm, $\Delta D = 0.1$ μm, and $D_0 = 1$ μm at $\lambda = 5.0$ μm. b,c) The simulated (top) and the measured (bottom) cross-section of the light field intensity in the X–Y plane for the bilayer flat lens with the period of $P = 1.3$ μm (b) and $P = 2.0$ μm (c).

an optical lens free from coma and spherical aberrations, the Abbe sine condition should be established which means the ratio between the sine of the angle of the ray radiated from the object and the sine of the angle of the same ray reaching to the image should be constant for the rays. The optical lens which is designed to overcome both spherical and coma aberrations is aplanatic lens which is patterned on a spherical interface and used commonly in optical microscopes.[34,48,49] Here, the double-layer flat lens can be modified as an aplanatic lens, such that the first layer is designed to behave like the spherical interface for the second layer. For the current design, since the first layer has a cylindrical focal line, under certain conditions, it can satisfy the Abbe sine condition and decrease the spherical and coma aberrations which are two different types of monochromatic aberrations.

2.5. Transmission Efficiency

A crucial parameter of any type of optical lens is the amount of incident light that is focused in the forward direction is called transmission efficiency of the lens. Conventional refractive lens based on CaF_2 can reach <95% up to $\lambda = 6$ μm and based on ZnSe can reach <70% up to $\lambda = 16$ μm [Janis Research Company, LLC]. However, our proposed plasmonic flat lens does not allow such high transmission efficiency due to the metallic loss but enable almost aberration-free subwavelength focusing with extremely low planar physical footprint ($<<\lambda$). As predicted in Figure 2b, the present design allows higher transmission efficiency with larger pattern period P due to the lower metallic fill-fraction. Furthermore, due to the reduced near-field and far-field interactions between plasmonic nanoantennas with the increase in period P, there is a red shift in the resonance wavelength pushing the lowest transmission at the resonance wavelength ($\lambda_{res} = 6.5$ μm) away from the designed wavelength ($\lambda = 5.0$ μm). However, the larger period P shifts the focal length to higher values due to the wider phase response distribution according to Equation (1) and the weakening of coupling between neighboring disks, as can be observed in Figure 2b.

Figure 6a overlays the simulated and the measured transmission efficiencies of the single-layer flat lenses with $P = 1.3$ μm (left) and $P = 2.0$ μm (right). Comparison of these two plots not only validates the simulated results but also proves that the increase in the period enhances the transmission efficiency, besides keeping the focusing effect, which is shown by the cross-section of field intensity in the y–z plane for different wavelengths. At the wavelengths above resonance, a broadband transmission efficiency higher than 60% is achieved, which is much higher compared with the other reported metasurface-based flat lenses operating in the mid-IR

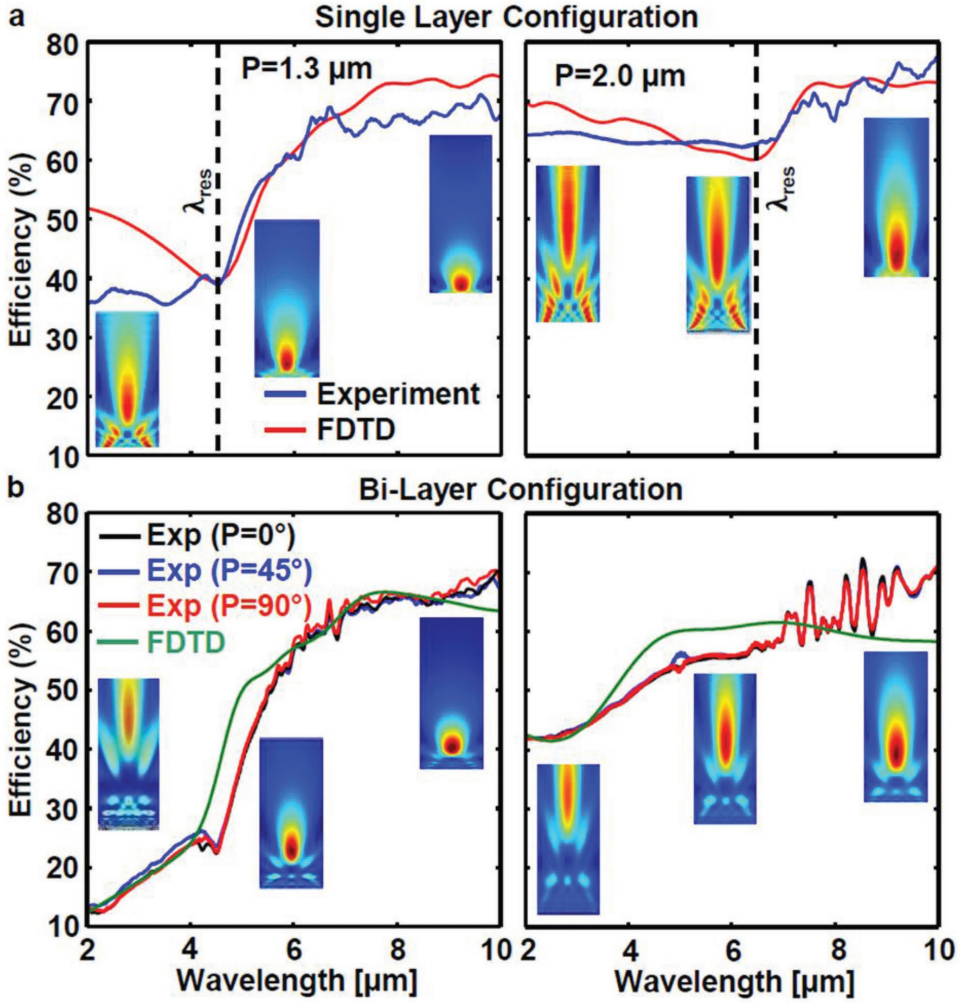

Figure 6. Transmission efficiency. a) The simulated (red) and the measured (blue) transmission efficiencies of the single-layer plasmonic lenses with the periods of $P = 1.3$ μm (left) and $P = 2.0$ μm (right). b) The simulated (green) and the measured (polarization = 0° (black), 45° (blue), and 90° (red)) transmission efficiencies of the bilayer plasmonic lenses with the periods of $P = 1.3$ μm (left) and $P = 2.0$ μm (right).

spectral range.[5,13] Figure 6b shows the measured transmission efficiency of the bilayer lens at the focal point for different linear-polarized incident light (pol = 0°, 45°, and 90°), which closely matches with the FDTD prediction of transmission of 0° linear-polarized light. Near perfect overlap between these plots further validates polarization independency of this bilayer lens. Minor discrepancies originate from the mismatch between the alignment of the two layers during fabrication compared with the simulated supercell. Similar to the single-layer plasmonic lens, the increase in the period P gives rise to higher transmission efficiency while maintaining focusing effect for the entire mid-IR wavelengths, as can be observed in Figure 6b. The bilayer flat lens acts like a spherical lens with ultrathin thickness (≈300 nm), the focal volume of which is further tunable by geometrical parameters of two independent layers over broad spectral range. In order to calculate the transmission efficiency from simulation and measurement, the incident light is taken as the reference, and the amount of light transmitted at the focal point with respect to that reference has been considered as the transmission efficiency. This means the reflection loss from the first interface of the substrate has been contributed in the efficiency calculation.

3. Conclusions

In conclusion, various planar lenses are demonstrated following the diffractive optics concept of phase control based on dielectric scatterers on a 2D plane. However, in the mid-infrared wavelength range (3–16 μm), such engineered dielectric surfaces are not possible due to the low spectral bandwidth and high thermal noise in long wavelengths. Plasmonic nanostructures enable abrupt change in phase, amplitude, and polarization of the incident light using subwavelength optical scatterer on a planar surface. We demonstrated a novel flat plasmonic lens based on gold in single and bilayer geometry to focus polarized and unpolarized light beams. The focal length and spot size are tunable with geometrical parameters providing design flexibility. The gradient design offers unique broadband near aberration-free operation unlike other flat lenses. High

transmission efficiency compared with the current flat lenses along with low FWHM of the focal point and ultrathin thickness make this lens a right candidate for the compact thermal imaging systems and photonic-integrated circuits.

4. Experimental Section

Simulation: The simulations were done by using FDTD method using the FDTD software (Lumerical, inc.).

Fabrication: The one-layer flat lens was patterned on a bilayer electron resist (MMA/PMMA) spin coated on silicon wafer (100 µm thickness), which had more than 70% transmission in mid-IR wavelengths, using electron beam lithography, developed in MIBK/IPA (3:1) following by deposition of Ti/Au (3 nm/45 nm) and lift-off process. Using a bilayer electron resist helped to lift-off the remaining resist without sonication and damaging the nanostructure. To fabricate the bilayer flat lens, after patterning MMA/PMMA on silicon (100 µm) substrate by EBL, following by Ti/Au (3 nm/45 nm) deposition and lift-off process, a layer of SU-8 polymer with thickness of 200 nm which had low light absorption in mid-IR was spin coated on the fabricated layer following by 2 h UV exposure and 1 h baking (95 °C) to become hard enough against polymer solvent (acetone) and decrease light absorption. A thin layer of Al_2O_3 (20 nm) was deposited on this layer to spin coat a uniform layer of MMA/PMMA on that and patterning it with electron-beam lithography (EBL). Due to the ease of interface finding, silicon wafer was used to fabricate the pattern using electron-beam lithography. But, it was possible to use an IR transparent substrate such as sapphire instead to increase the light transmission to more than 95%. To fabricate the pattern on top of that, the nanoimprint lithography could be used to decrease the cost and increase throughput. Four markers were used to write the next layer exactly 90° rotated with respect to the first layer. Another Ti/Au (3 nm/45 nm) deposition and lift-off process was done to prepare the bilayer flat lens.

Measurement: In the confocal measurement, the 3D field intensity of the focal point was scanned by using a 3D automatic motor. A bandpass filter for $\lambda = 5.0$ µm with the bandwidth of 70 nm along with a linear polarizer was located in front of the infrared source of FTIR. An aspheric lens with low numerical aperture (NA = 0.2) was used to focus the light beam uniformly on the sample which was attached to a 3D automatic motor. A high NA aspheric lens (NA = 0.9) between two confocal pinholes was utilized to collect the transmitted photons and send them to a cooled MCT. The scanning, measurement, and motor motion were controlled by a Labview program.

Supporting Information

Supporting Information is available from the Wiley Online Library or from the author.

Acknowledgements

A.S. conceived the idea. A.S. designed and performed the experiments. A.V.G. and D.F. provided technical assistance. A.S. and D.C. analyzed and simulated the data. A.S., M.L., and D.C. contributed materials/analysis tools. A.S. and D.C. cowrote the paper. This work at the University of Central Florida was partially supported by DARPA under the WIRED program grant no. HR0011-16-1-0003, the University research program of Northrop Grumman under the grant no. 63018088.

Conflict of Interest

The authors declare no conflict of interest.

Keywords

Abbe-Rayleigh diffraction limit, geometric tunability, localized surface plasmons, mid-infrared spectral domain, optical lens, polarization dependency

Received: February 18, 2018
Revised: March 10, 2018
Published online:

[1] E. Hecht, *Optics*, 4th ed., Addison Wesley, Boston **2002**.
[2] F. M. Huang, N. I. Zheludev, *Nano Lett.* **2009**, *9*, 1249.
[3] D. Fattal, J. J. Li, Z. Peng, M. Fiorentino, R. G. Beausoleil, *Nat. Photonics* **2010**, *4*, 466.
[4] D. Lin, P. Fan, E. Hasman, M. L. Brongersma, *Science* **2014**, *345*, 298.
[5] N. Yu, F. Capasso, *Nat. Mater.* **2014**, *13*, 139.
[6] L. F. Zou, W. Withayachumnankul, C. M. Shah, A. Mitchell, M. Bhaskaran, S. Sriram, C. Fumeaux, *Opt. Express* **2013**, *21*, 1344.
[7] M. Khorasaninejad, W. T. Chen, A. Y. Zhu, J. Oh, R. C. Devlin, C. Roques-Carmes, I. Mishra, F. Capasso, *IEEE J. Sel. Top. Quantum Electron.* **2017**, *23*, 4700216.
[8] H. Zuo, D.-Y. Choi, X. Gai, P. Ma, L. Xu, D. N. Neshev, B. Zhang, B. Luther-Davies, *Adv. Opt. Mater.* **2017**, *5*, 1700585.
[9] A. Arbabi, R. M. Briggs, Y. Horie, M. Bagheri, A. Faraon, *Opt. Express* **2015**, *23*, 33310.
[10] R. D. Hudson Jr., *Infrared System Engineering*, 1st ed., John Wiley & Sons, Hoboken, New Jersey **2006**.
[11] J. J. Talghader, A. S. Gawarikar, R. P. Shea, *Light: Sci. Appl.* **2012**, *1*, e24.
[12] V. Giannini, A. I. Fernandez-Dominguez, S. C. Heck, S. A. Maier, *Chem. Rev.* **2011**, *111*, 3888.
[13] Y. Fu, X. Zhou, *Plasmonics* **2010**, *5*, 287.
[14] N. Yu, P. Genevet, M. A. Kats, F. Aieta, J. P. Tetienne, F. Capasso, Z. Gaburro, *Science* **2011**, *334*, 333.
[15] X. Ni, N. K. Emani, A. V. Kildishev, A. Boltasseva, V. M. Shalaev, *Science* **2012**, *335*, 427.
[16] N. Yu, F. Aieta, P. Genevet, M. A. Kats, Z. Gaburro, F. Capasso, *Nano Lett.* **2012**, *12*, 6328.
[17] O. Akin, H. V. Demir, *Opt. Express* **2015**, *23*, 27020.
[18] C. Pfeiffer, A. Grbic, *Phys. Rev. Lett.* **2013**, *110*, 197401.
[19] W. L. Barnes, A. Dereux, T. W. Ebbesen, *Nature* **2003**, *424*, 824.
[20] H. J. Lezec, A. Degiron, E. Devaux, R. A. Linke, L. Martin-Moreno, F. J. Garcia-Vidal, T. W. Ebbesen, *Science* **2002**, *297*, 820.
[21] M. Khorasaninejad, W. T. Chen, R. C. Devlin, J. Oh, A. Y. Zhu, F. Capasso, *Science* **2016**, *352*, 1190.
[22] N. Fang, H. Lee, C. Sun, X. Zhang, *Science* **2005**, *308*, 534.
[23] A. Vazquez-Guardado, A. Safaei, S. Modak, D. Franklin, D. Chanda, *Phys. Rev. Lett.* **2014**, *113*, 263902.
[24] S. Larouche, D. R. Smith, *Opt. Lett.* **2012**, *37*, 2391.
[25] P. Biagioni, M. Savoini, J.-S. Huang, L. Duò, M. Finazzi, B. Hecht, *Phys. Rev. B* **2009**, *80*, 045411.
[26] J. P. Tetienne, R. Blanchard, N. Yu, P. Genevet, M. A. Kats, J. A. Fan, T. Edamura, S. Furuta, M. Yamanishi, F. Capasso, *New J. Phys.* **2011**, *13*, 053057.
[27] E. Verhagen, A. Polman, L. K. Kuipers, *Opt. Express* **2008**, *16*, 45.
[28] A. Niv, G. Biener, V. Kleiner, E. Hasman, *Opt. Commun.* **2005**, *251*, 306.
[29] B. Gjonaj, J. Aulbach, P. M. Johnson, A. P. Mosk, L. Kuipers, A. Lagendijk, *Phys. Rev. Lett.* **2013**, *110*, 266804.
[30] Y. Zhang, Y. Fu, X. Zhou, *Insci. J.* **2011**, *1*, 18.
[31] W. Srituravanich, L. Pan, Y. Wang, C. Sun, D. B. Bogy, X. Zhang, *Nat. Nanotechnol.* **2008**, *3*, 733.

[32] J. Hu, C. H. Liu, X. Ren, L. J. Lauhon, T. W. Odom, *ACS Nano* **2016**, *10*, 10275.
[33] J. Lin, J. P. Mueller, Q. Wang, G. Yuan, N. Antoniou, X. C. Yuan, F. Capasso, *Science* **2013**, *340*, 331.
[34] F. Aieta, P. Genevet, N. Yu, M. A. Kats, Z. Gaburro, F. Capasso, *Nano Lett.* **2012**, *12*, 1702.
[35] X. Ni, S. Ishii, A. V. Kildishev, V. M. Shalaev, *Light: Sci. Appl.* **2013**, *2*, e72.
[36] A. Pors, M. G. Nielsen, R. L. Eriksen, S. I. Bozhevolnyi, *Nano Lett.* **2013**, *13*, 829.
[37] A. Safaei, S. Chandra, A. Vázquez-Guardado, J. Calderon, D. Franklin, L. Tetard, L. Zhai, M. N. Leuenberger, D. Chanda, *Phys. Rev. B* **2017**, *96*, 165431.
[38] H. P. Paudel, A. Safaei, M. N. Leuenberger, in *Metallic Nanostructures and Dirac Systems* (Ed: D. G. Barbillon), InTech, London **2017**.
[39] L. Verslegers, P. B. Catrysse, Z. Yu, J. S. White, E. S. Barnard, M. L. Brongersma, S. Fan, *Nano Lett.* **2009**, *9*, 235.
[40] J. D. Jackson, *Classical Electrodynamics*, 3th ed., John Wiley & Sons, Hoboken, New Jersey **1998**.
[41] A. B. Evlyukhin, G. Brucoli, L. Martin-Moreno, S. I. Bozhevolnyi, F. J. Garcia-Vidal, *Phys. Rev. B* **2007**, *76*, 075426.
[42] O. J. Martin, C. Girard, A. Dereux, *Phys. Rev. Lett.* **1995**, *74*, 526.
[43] A. B. Evlyukhin, C. Reinhardt, E. Evlyukhin, B. N. Chichkov, *J. Opt. Soc. Am. B* **2013**, *30*, 2589.
[44] S. Modak, A. Safaei, D. Chanda, arXiv, 1710.00392 **2017**.
[45] C. F. Bohren, D. R. Huffman, *Absorption and Scattering of Light by Small Particles*, John Wiley & Sons, Hoboken, New Jersey **1998**.
[46] F. Aieta, P. Genevet, M. A. Kats, N. Yu, R. Blanchard, Z. Gaburro, F. Capasso, *Nano Lett.* **2012**, *12*, 4932.
[47] P. Wang, N. Mohammad, R. Menon, *Sci. Rep.* **2016**, *6*, 21545.
[48] D. B. Murphy, M. W. Davidson, *Fundamentals of Light Microscopy and Electronic Imaging*, 2nd ed., John Wiley & Sons, Hoboken, New Jersey **2009**.
[49] F. Aieta, P. Genevet, M. Kats, F. Capasso, *Opt. Express* **2013**, *21*, 31530.

